

From rogue wave solution to solitons

Amdad Chowdury ¹, Wonkeun Chang ², and Marco Battiato¹

¹*School of Physical and Mathematical Sciences, Nanyang Technological University, 637371 Singapore*

²*School of Electrical and Electronic Engineering, Nanyang Technological University, 639798 Singapore*



(Received 21 July 2022; accepted 8 January 2023; published 23 January 2023)

Using a generalized nonlinear Schrödinger equation, we investigate the transformation of a fundamental rogue wave solution to a collection of solitons. Taking the third-order dispersion, self-steepening, and Raman-induced self-frequency shift as the generalizing effects, we systematically observe how a fundamental rogue wave has an impact on its surrounding continuous wave background and reshapes its own characteristics while a group of solitons are created. Applying a local inverse scattering technique based on the periodization of an isolated structure, we show that the third-order dispersion and Raman-induced self-frequency shift generates a group of solitons in the neighborhood where the rogue wave solution emerges. Using a volume interpretation, we show that the self-steepening effect stretches the rogue wave solution by reducing its volume. Also, we find that with the Raman-induced self-frequency shift, a decelerating rogue wave generates a red-shifted Raman radiation while the rogue wave itself turns into a slow-moving soliton. We show that when third-order dispersion, self-steepening, and Raman-induced self-frequency shift act together on the rogue wave solution, each of these effects favor the rogue wave to generate a group of solitons near where it first emerges while the rogue wave itself also becomes one of these solitons.

DOI: [10.1103/PhysRevE.107.014212](https://doi.org/10.1103/PhysRevE.107.014212)

I. INTRODUCTION

After the discovery of a rogue wave solution in a nonlinear Schrödinger equation (NLSE) by D. H. Peregrine in 1984, there was a surge of interest because of its ability to explain the formation of a sudden giant oceanic wave, which is often called a rogue wave or a monster of the deep [1]. While at the beginning, most of the investigations were focused on applying the solution to oceanic rogue waves [2–4], the idea has gradually expanded to other fields such as nonlinear optics [5], plasma physics [6], atmospheric science [7], superfluids [8], Bose-Einstein condensates [9], capillary waves [10], acoustic waves [11,12], electromagnetic waves [13], matter waves [14], and economics [15].

Among many systems where the concept of rogue wave formation is materialized, hydrodynamics and optics are the two areas where most new discoveries are made. This is because both water and optical fiber possess dispersive and nonlinear properties that can be modeled by the NLSE. Note that two nonequivalent definitions of rogue waves are commonly used in the literature. In the first definition, the rogue wave solution is derived from a periodic breather solution of the NLSE [16]. When the period becomes infinite, the single peak rogue wave solution emerges [17]. Most of the salient features of this solution can be observed in rogue waves in various chaotic systems [18]. Such definition is not equivalent to the statistical description of rogue waves which is widely used in the historical oceanographic case alone [19]. For the sake of brevity, rogue waves in the rest of the article refer to rogue wave solutions.

The presence of rogue waves in optics and hydrodynamics has been confirmed experimentally [5,20,21]. Thus, rogue

wave observations can now be made in a water-wave tank or on an optical table. In particular, due to the wide availability of various optical components, the research on optical rogue waves became popular since its discovery 14 years ago [20]. A comprehensive overview of the recent progress in optical rogue wave research can be found in Refs. [17,22,23].

The basic form of a NLSE has limitations when modeling ultrashort pulse propagation, as it can trigger higher-order linear and nonlinear optical effects [24,25]. Among them, the third-order dispersion (TOD), self-steepening (SS), and Raman-induced self-frequency shift (RIFS) are the most dominant mechanisms that can directly affect the pulse. The inclusion of these terms in the NLSE destroys its integrability, and hence a majority of theoretical studies of their effect on optical rogue waves so far have been carried out either numerically or by taking only one or two effects at a time. The result is an incomplete picture of the rogue wave dynamics under these higher-order effects. Moreover, many studies focus only on how these effects impact the central structure of the rogue wave solutions or whether the solutions can survive the perturbations [26–29], and little effort has been made to understand their impact on the neighboring continuous wave background. The modulation instability (MI) which generates rogue wavelike structures creates a variety of other substructures originating from this continuous wave background. This is apparent in a MI-based supercontinuum generation, where a long pulse undergoes MI, and the end product is a shower of hundreds of fundamental solitons [30,31]. How these soliton bunches are formed in the midst of MI has not yet been clearly described.

In this article, we conduct a comprehensive study on the temporal and spectral properties of an optical rogue wave in

the generalized nonlinear Schrödinger equation (GNLSE) that includes TOD, SS, and RIFS effects. By first taking individual effects separately, we study how each one impacts the rogue wave solution in the temporal and spectral domains *at the time of the rogue wave appearance*. We also present what changes these three effects produce on the surrounding waves *after the emergence of the rogue wave* and the fate of the rogue wave after it evolves for a long time. Finally, we apply the three effects simultaneously and observe the combined evolution characteristics. Employing numerical simulations complimented with a local-inverse scattering transformation technique (IST) [32] based on the periodization of isolated structures from the chaotic wave field, we find that a fundamental rogue wave triggers a collection of solitons from its emerging point while the rogue wave itself also transforms into a soliton under the influence of TOD, SS, and RIFS effects.

A. Model, solution, and techniques

The GNLSE in its normalized form is [24]

$$\begin{aligned} i \frac{\partial \psi}{\partial z} - \frac{\beta_2}{2} \frac{\partial^2 \psi}{\partial t^2} + \gamma \psi |\psi|^2 \\ = i\epsilon_3 \frac{\partial^3 \psi}{\partial t^3} - is \frac{\partial}{\partial t} (\psi |\psi|^2) + \tau_R \psi \frac{\partial |\psi|^2}{\partial t}, \end{aligned} \quad (1)$$

where β_2 , γ , ϵ_3 , s , and τ_R are the normalized coefficients of the group-velocity dispersion, optical Kerr effect, TOD, SS, and RIFS, respectively. The explicit expressions of the coefficients in Eq. (1) are

$$\epsilon_3 = \frac{\beta_3}{6|\beta_2|t_0}, s = \frac{1}{\omega_0 t_0}, \tau_R = \frac{T_r}{t_0},$$

where ω_0 is the carrier angular frequency, t_0 is the pulse duration, β_3 the TOD parameter, and T_r is the Raman time constant [33]. The TOD, SS, and RIFS effects are inversely proportional to the pulse duration t_0 , i.e., their contributions can be negligible when t_0 is large, or significant when it is small. Setting $\epsilon_3 = s = \tau_R = 0$, $\beta_2 = -1$, and $\gamma = 1$, Eq. (1) becomes NLSE, which can be solved analytically using the standard-IST [34]. Note that the standard-IST can be used to construct entire solutions for all z and t , whereas local-IST can be employed to determine the IST spectrum of an isolated localized structure, which only requires the t -dependent part of the NLSE Lax-pair [32]. In this article, we apply the local-IST procedure for all observations.

We assume that TOD, SS, and RIFS are the perturbations to the NLSE. We take small values of these effects and study their impact on the rogue wave dynamics. To find numerical solutions in the perturbed system, we pick an initial condition from the exact analytical first-order rogue wave solution of NLSE, which is given as

$$\psi(z, t) = \left[1 - \frac{G + iH(z - z_1)}{D} \right] e^{i(z - z_1)}. \quad (2)$$

The solution can be derived by applying the Darboux transformation technique using the plane wave $\psi = \exp(iz)$ as an initial seed solution where $G = 4$, $H = 8$, and $D = 1 + 4t^2 + 4(z - z_1)^2$ [35]. The initial condition in our study should start practically from a minuscule amplitude that works as an infinitesimally small modulation on the background. Therefore,

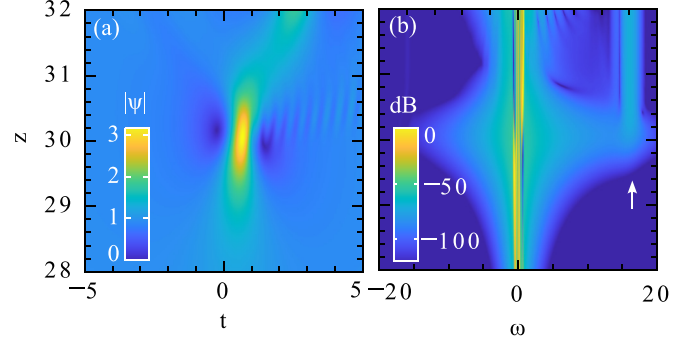


FIG. 1. (a) Temporal amplitude evolution of the emergence of a first-order rogue wave at $z = 30$ with $\epsilon_3 = -0.03$ (b) Corresponding spectral intensity evolution. It shows the emission of dispersive wave shown by the white arrow as observed in Ref. [39]. Note that in the analytic solution, the rogue wave appears at $z = 0$ where as in simulation it is at $z = 30$.

we use the solution well before it emerges into a full-height rogue wave; i.e., we set $z_1 = 30$. These effects exponentially amplify the small modulation which eventually appears as a rogue wave solution. The details of the numerical techniques applied to solve the perturbed NLSE-type equation are provided in Ref. [36].

In a chaotic wave field, various types of wave coexist together such as plane waves, solitons, and breathers. The local-IST technique is a useful mean to classify a random wave field into these types. We use it to identify the types of waves formed on top of the background wave when NLSE is perturbed. This involves finding the eigenvalues of a given potential as a particular wave form, which provides a spectral portraits of soliton-type solutions. The local-IST spectral problem is generally solved in the framework of finite-gap theory [32]. Depending on a given spectral portrait, the genus, g , identifies what type of solution the spectrum belongs to. g is measured as $J - 1$, where J is the number of spectral bands in the spectrum. The rogue-wave-type solutions have $g = 2$ as they have three spectral bands. The plane waves have $g = 0$, while the soliton solutions have $g = 1$. The details of the use of local-IST techniques to classify various localized wave forms are discussed in Refs. [32,37,38]. Note that to resolve the spectral identity and to determine the genus of localized structures, we follow the framework employed in Ref. [38] (e.g., see Figs. 2 and 7).

II. EFFECT OF THIRD-ORDER DISPERSION

Taking the effect of TOD only, the generalized NLSE takes the form

$$i \frac{\partial \psi}{\partial z} + \frac{1}{2} \frac{\partial^2 \psi}{\partial t^2} + \psi |\psi|^2 - i\epsilon_3 \frac{\partial^3 \psi}{\partial t^3} = 0. \quad (3)$$

No analytic rogue wave solutions exist for the NLSE with the TOD term. Numerical descriptions of the rogue wave solutions in wave turbulence have been presented in Refs. [40,41]. Similarly, the dispersive wave emission from a rogue wave as a result of TOD, shown in Fig. 1 indicated by the white arrow, has been demonstrated in Ref. [39]. The rogue wave emerges at around $z = 30$ in Fig. 1 with a drift velocity while

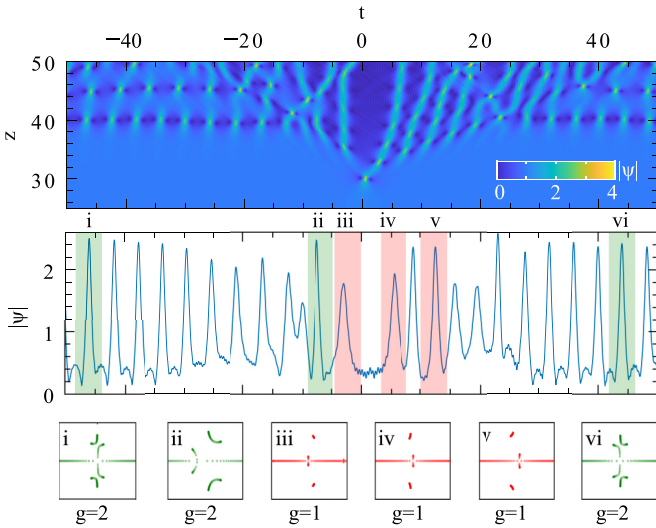


FIG. 2. Top panel: Temporal amplitude evolution of a rogue wave under the influence of TOD. The rogue wave appears at $z = 30$, and a skewed background wave dynamics is visible with a combination of different types of wave entities. Midpanel: The wave envelop is an instance extracted at $z = 40$ after the emergence of the rogue wave. Bottom panel: Local-IST spectra of various types of wave profiles.

radiating a phase-matched dispersive wave following the relation $\omega_{DW} = 3/\beta_3$. A similar type of radiation also occurs when higher-order soliton is perturbed by TOD [42].

TOD has a significant influence on the surrounding wave environment as well as reshaping the rogue wave while it evolves for a long time. Our earlier study [36] indicated that TOD transforms a rogue wave eventually to a collection of solitons. It is the lateral evolution of the rogue wave after its development that gives rise to the soliton-type waves. For instance, as shown in Fig. 2 (top panel), the background waves are creating a host of various other types of waves beyond the point of the rogue wave emergence at $z = 30$ as a result of TOD.

To identify the types of waves generated, we use the local-IST technique for spectral analyses. We take an instances of the solution at $z = 40$ after the emergence of the rogue wave in Fig. 2 and choose six localized formations from the profile presented in the midpanel. There are two types of waves formed, breather and soliton-types, which are grouped by green and red shaded areas. As indicated in the insets (bottom panel), the entire transverse profile reveals IST spectra of solitons with the appearance of breathers and new rogue waves. Note that the rogue wave is also a class of breather-type solution. The breather or $g = 2$ -type solution arises near the edges of the field showing three distinct IST-spectral bands in insets i, ii, and vi. Soliton-type structures arise in the middle of the profile, where they are ejected from near the emerging point of the rogue wave at $z = 30$.

To be exact, the local-IST spectra in insets iii, iv, and v show three spectral bands. However, the small-amplitude bands crossing the real line arise due to the background perturbation, which are not as extended as in insets i, ii, and vi. Thus, the local IST-spectra in iii, iv, and v are of two complex

conjugate bands making them approximately $g = 1$ -type soliton [38]. This shows that TOD has a direct influence on the rogue wave, transforming it toward solitons.

III. EFFECT OF SELF-STEEPENING

To observe the change arising from the SS term on a rogue wave, we consider the equation

$$i \frac{\partial \psi}{\partial z} - \frac{\beta_2}{2} \frac{\partial^2 \psi}{\partial t^2} + \gamma \psi |\psi|^2 + is \frac{\partial}{\partial t} (\psi |\psi|^2) = 0. \quad (4)$$

We note that analytic rogue wave solutions of the derivative NLSE, which is similar to Eq. (4), have been derived and discussed in several previous works [43–45]. These solutions can be converted to the rogue wave solutions of Eq. (4) through a gauge transformation [43]. However, this makes it difficult to observe the solutions in the limit of $s \rightarrow 0$, as the coefficient s appears in the solution with an inverse relation, making them indeterminate at a small s [43,46].

We look for a solution that can be studied without this restriction. We reformulate the rogue wave solution of the modified NLSE presented in Refs. [47,48] into a simpler form, revealing its clear connection with the NLSE rogue wave solutions. This is given as

$$\psi_s(z, t) = \left(1 - \frac{G + iHz + 8is\tau}{D_s} \right) e^{i[z(1+\frac{1}{2}s^2) - t\tau + \Phi]}, \quad (5)$$

where $\tau = t - zs$, $\kappa = 1 + s^2$, and

$$D_s = D + 4is(2\tau - t) + 4s\tau(s\tau - 2z),$$

$$\Phi = 2 \tan^{-1} \left[\frac{4s(zs - \tau)}{1 + 4\kappa(z^2 + \tau^2)} \right].$$

Here, $\beta_2 = -1$ and $\gamma = 1$, while s can be an arbitrary value. Now s arises in a way that the solution is not indeterminate as $s \rightarrow 0$ but, rather, it directly reduces to the fundamental rogue wave solution in Eq. (2). Equation (5) tells exactly how the SS term modifies the fundamental rogue wave solution. The denominator D_s is a complex polynomial which is real for a fundamental rogue wave solution. This solution profile can now be translated to any point on the z - t plane following the relations $t = t_1 - t_s$ and $z = z_1 - z_s$.

The broken symmetry in the solution is captured in the parameter s . The seed modulation acquires a velocity in the transverse direction at the initial stage of the rogue wave development. It gives rise to a new term $\tau = t - zs$, where s introduces the velocity as shown in Fig. 3. With $s = 0$, $\tau = t$, and eliminating the velocity component, Eq. (5) directly reduces to the fundamental rogue wave solution of the NLSE.

The effect of s on the rogue wave can be best described by the volume of the rogue wave. The volume is given by [49,50]

$$V = \frac{1}{8\pi} \int_{-\infty}^{\infty} \int_{-\infty}^{\infty} I_s(z, t)^2 dt dz, \quad (6)$$

where the intensity solution, $I_s(z, t) = (|\psi_s|^2 - 1)$, in the integral can be given as

$$I_s(z, t) = \frac{8[1 - 4t^2 + 8ts(z + s\tau) + 4(z - s\tau)(z + 3s\tau)]}{D_g D_g^*},$$

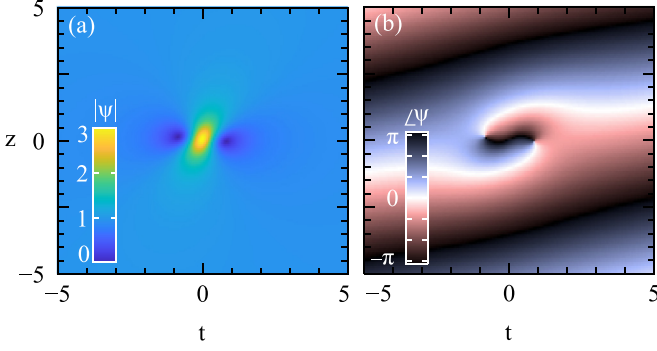


FIG. 3. (a) Amplitude and (b) phase profiles of the rogue wave from Eq. (5), with $s = 0.2$. It has a maximum amplitude of 3 with a distorted phase shift of π across the peak.

where $D_g = 1 + 4t^2 + 4its - 8is\tau + 4(z - s\tau)^2$, and D_g^* is its complex conjugate. From this, we obtain the volume V and the rate of volume change with respect to s , which are

$$V = \frac{1}{1 + s^2}, \quad \frac{dV}{ds} = -\frac{2s}{(1 + s^2)^2}. \quad (7)$$

We subtract the background amplitude 1 in the integral to avoid having infinite energy from the intensity solution. It is clear that the volume of a rogue wave under the influence of SS effect is varying with the coefficient s . A rogue wave is localized both in space (t) and time (z), and therefore V must be finite.

From Fig. 4(a), we have a finite volume of 1 when $s = 0$, which is the volume of fundamental rogue wave. With an increasing s , rogue wave's volume V decreases asymptotically. What this means in the rogue wave behavior is evident in Fig. 4(b). When $s = 2$, the rogue wave is stretched in the t dimension, creating an elongated profile with $V = 0.2$. At a larger value of s , this elongation increases with a small V , keeping the center amplitude 3 unchanged. The more stretched the rogue wave becomes, the less volume it can contain. A rogue wave with a large SS effect ($s \gg 1$) becomes an infinitely extended horizontal entity with $V \approx 0$.

Note that, in a real system, s generally remains small, hence the dynamics remain within a stretched and small volume ($V < 1$) rogue wave-type entity. When the SS effect with a small s value acts upon a rogue wave with other asymmetrical optical effects, it works like a strong stimulus, steering the

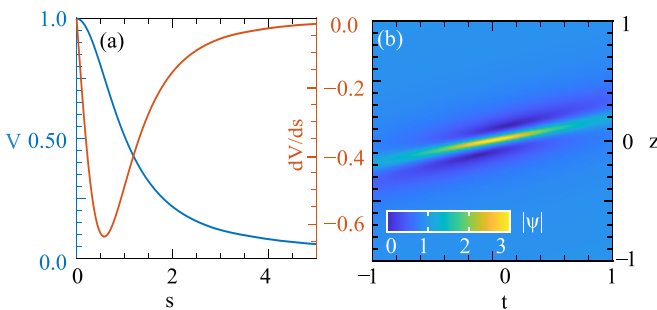


FIG. 4. (a) Rogue wave volume V (blue) and the rate of volume change dV/ds (red) versus s . (b) Onset of a rogue wave departing from its original state to become a soliton when $s = 2$.

rogue wave toward a soliton. The rate of change of volume as a function of s is also plotted in Fig. 4(a). The fastest change is observed at $s = 0.58$ with $dV/ds = -0.65$.

A. Effects on phase and spectral evolution

The SS term also induces a significant change in the rogue wave's temporal phase and spectral intensity. This term in Eq. (4) is a first-order t derivative of the self-phase modulation implying that instead of a π phase shift for NLSE rogue wave, the phase is varying in the transverse t dimension. Due to this, an asymmetric phase term Φ arises in the NLSE rogue wave solution. From Eq. (5), this can be given as

$$e^{i\Phi} = \frac{D_s^*}{D_s}, \quad (8)$$

which indicates that the asymmetrical phase profile has its origin in the denominator of the rational solution Eq. (5). The t varying phase means an instantaneous frequency changes across the envelope. The origin of this change comes from the SS term, which in the Fourier domain becomes $\frac{\partial}{\partial t}(\psi|\psi|^2) = -i\omega(\psi|\psi|^2)$, replacing $\partial/\partial t = -i\omega$. To deal with this type of asymmetric spectrum, a Heaviside step function is required, which makes the full derivation with arbitrary s , z , and t rather complicated. We take the Fourier transformation of Eq. (5) at $z = 0$:

$$F(\omega, s, z = 0) = \frac{1}{\sqrt{2\pi}} \int_{-\infty}^{\infty} \psi_s(z = 0, t) e^{i\omega t} dt. \quad (9)$$

For a fundamental rogue wave with $s = 0$, the spectrum is

$$F(\omega, s = 0, z = 0) = \sqrt{2\pi} [-e^{-\frac{|\omega|}{2}} + \delta(\omega)], \quad (10)$$

where δ is the Kronecker delta. For $s = 0.2$, the expression becomes

$$\begin{aligned} F(\omega, s = 0.2, z = 0) &= 5\sqrt{2\pi}\delta(1 - 5\omega) \\ &- \frac{1}{1521} \left\{ 25e^{-\frac{1}{52}(-1+3\sqrt{3})(-1+5\omega)} \sqrt{\frac{\pi}{2}}(5 + \omega) \right. \\ &\times \left. [a_1\theta(0.2 - \omega)e^{\frac{3}{26}\sqrt{3}(-1+5\omega)} + a_2\theta(-0.2 + \omega)] \right\}, \end{aligned}$$

where $a_1 = (9 + 14\sqrt{3})$, $a_2 = (-9 + 14\sqrt{3})$, and θ is a Heaviside step function. Similar spectral expressions can be derived for any values of s . For simplicity, we omit the cumbersome mathematical expressions.

The impact of the SS effect on the phase and spectrum for all z and t is demonstrated in Fig. 5 using the solution presented in Eq. (5). In Fig. 5(a), the flat-top π phase shift for the fundamental rogue wave with $s = 0$ is now distorted in Figs. 5(c) and 5(e) for $s = 0.2$ and 1, respectively. As a result, the corresponding asymmetrical spectral intensity broadening is observed around $\psi(z = 0, t = 0)$ which shown in Figs. 5(d) and 5(f). Note that with $s = 0$, the spectrum becomes triangular, which represents a rogue wave, as shown in Fig. 5(b). With an increasing s , the spectral profile broadens asymmetrically toward the blue side. The maximum phase distortion is seen when $s = 1$, which is accompanied by the widest spectral bandwidth.

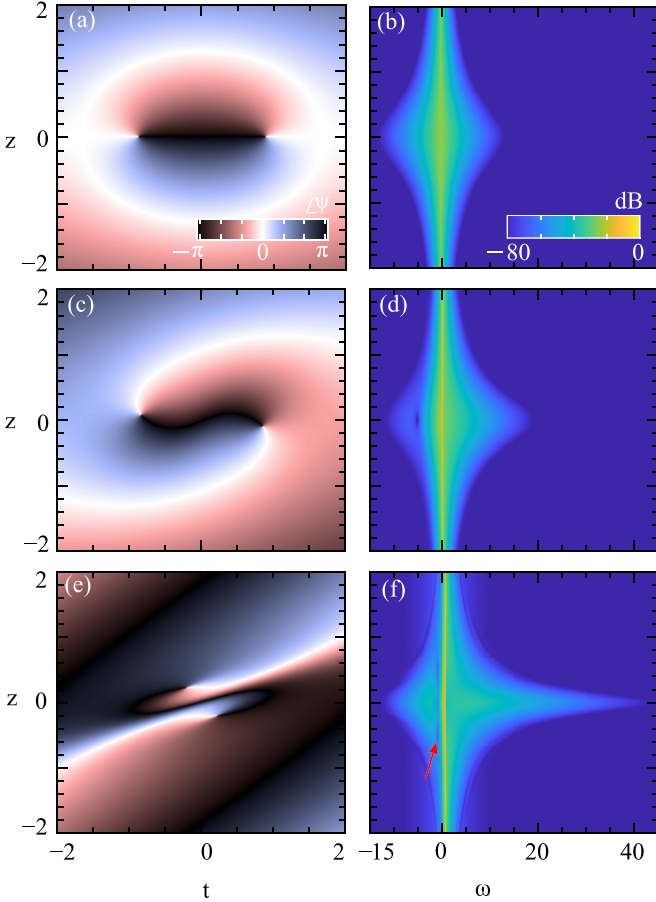


FIG. 5. (a) Temporal phase and (b) spectral intensity evolutions of the rogue wave solution, Eq. (5) with $s = 0, 0.2$, and 1 . Note a spectral discontinuity is arise in the spectrum indicated by the red arrow.

B. Extended evolution and translation

To investigate how the SS effect influences the background after the emergence of the rogue wave, we simulate the fundamental rogue wave for an extended propagation length. The evolution is presented in Fig. 6. It induces a skewed asymmetry in the recurring breathers after the emergence of the rogue wave. Unlike the effects of TOD, no solitary waves nor dispersive waves are observed in the neighborhood.

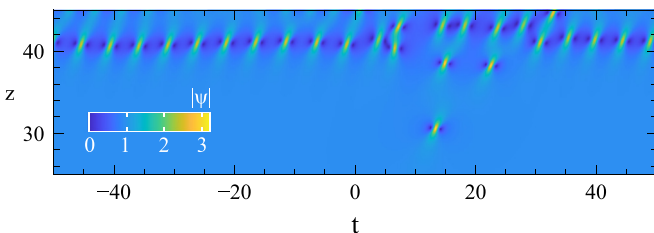


FIG. 6. (a) Extended amplitude evolution of a rogue wave with the SS effect when $s = 0.2$. The recurring emergence of breathers is also achieved with the same amount of translations as the primary rogue wave. The rogue wave has appeared at a translated distance $t \approx 13$.

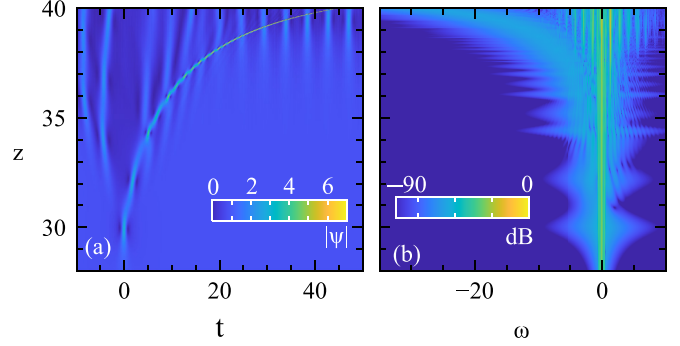


FIG. 7. (a) Temporal and (b) spectral intensity evolutions of a fundamental rogue wave under the influence of RIFS effect when $\tau_R = 0.012$. The rogue wave appearing at $z = 30$ is decelerating along the propagation. A frequency down-shifting is observed in the spectral domain.

Another important aspect of our current observation with the SS effect is the fundamental rogue wave solution Eq. (2) undergoes a natural translation on the z - t plane. We observe that instead of the rogue wave appearing at $t = 0$, it emerges translated at $t \approx 13$ when $s = 0.2$. This indicates that the translational parameter t_s in the analytic solution Eq. (5) is naturally triggered by the finite s in the system. We observe that in the analytic solution, the same amount of translation can be achieve by setting $t_s = 13$ and $z_s = 0$.

IV. ROGUE WAVE SELF-FREQUENCY SHIFT

To investigate the RIFS effect on a rogue wave, we employ

$$i \frac{\partial \psi}{\partial z} - \frac{\beta_2}{2} \frac{\partial^2 \psi}{\partial t^2} + \gamma \psi |\psi|^2 - \tau_R \psi \frac{\partial |\psi|^2}{\partial t} = 0. \quad (11)$$

The Raman term in Eq. (11) is a non-Hamiltonian dissipative term [51]. Therefore, Eq. (11) does not render an analytical solution, and the study is undertaken numerically. Our investigation shows that the RIFS effect does not impact the main rogue wave solution structure in a significant way keeping the amplitude and phase profiles unaltered. However, the impact becomes significant after the emergence of the rogue wave. The RIFS effect mainly induces a steering effect on the rogue wave slowing it down in a transverse direction and gradually transforms it into a soliton.

Since the RIFS parameter τ_R is inversely proportional to the pulse duration, its role becomes greater when the rogue wave reaches the maximum compression point. The dissipative nature of the RIFS effect means that the solution does not preserve the energy. As shown in Fig. 7, when the rogue wave solution is maximally compressed, its bandwidth is wide enough to amplify the low-frequency components at the expense of the blue-side. At this stage, the rogue wave is no longer robust, but instead it loses energy by generating red spectral components. As the energy dissipation continues, the rogue wave slows down and decelerates. Each time the rogue wave appears with less energy, the compression becomes strong, resulting in a broader spectrum as shown in Fig. 7(b). Note that the RIFS-induced radiation in the red side appears to be small in the first few rogue wave events along z . This means

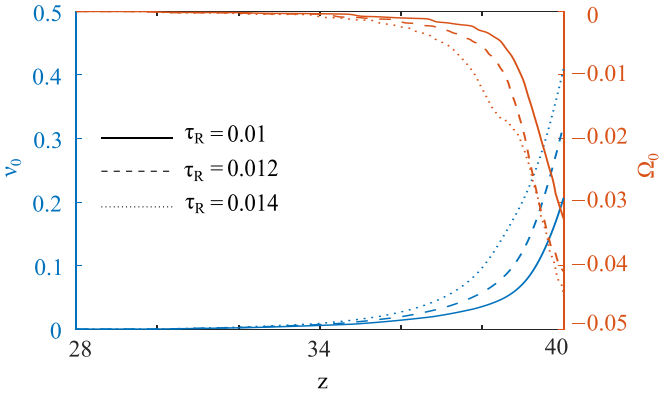


FIG. 8. Trajectories of the center of mass of the rogue wave solution in the temporal (blue) and spectral (red) domains under the influence of RIFS effect.

that the pulse duration in the first few rogue wave emergences are still not short enough to fully activate the RIFS effect.

The propagation dynamics can be more effectively described by the progression of the center of mass of rogue wave solution while it is under the influence of RIFS effect. The centers of mass in temporal and spectral amplitudes, v_0 and Ω_0 , are defined as

$$v_0 = \frac{\int_{-\infty}^{\infty} t |\psi(z, t)|^2 dt}{\int_{-\infty}^{\infty} |\psi(z, t)|^2 dt}, \quad \Omega_0 = \frac{\int_{-\infty}^{\infty} \omega |\psi(z, \omega)|^2 d\omega}{\int_{-\infty}^{\infty} |\psi(z, \omega)|^2 d\omega}. \quad (12)$$

Figure 8 shows the trajectories for three different values of the RIFS coefficient, $\tau_R = 0.010, 0.012,$ and 0.014 . For high values of τ_R , the magnitude of RIFS is also large. With this, the spectrum shifts toward the negative frequency side along the propagation. This results in the rogue wave slowing down in the temporal domain, making an increasingly skewed bow-shaped trail.

We carry out simulations for a longer distance of $z = 50$ to investigate the fate of the rogue wave after an extended propagation and its impacts on the neighboring wave field. This is shown in the top panel of Fig. 9. We can see that after its appearance at $z = 30$, the rogue wave triggers a group of solitons at the central region similar to TOD while its trajectory bends toward the positive t direction. As the propagation progresses, the continuous dissipation of energy significantly reduces its velocity and gradually becomes a meandering high-amplitude solitonlike entity. Note that before transforming to a soliton, in the initial stage the decelerating rogue wave collides multiple times with neighboring other solitons and breather-type substructures, leading to a higher amplitude soliton [52].

The rogue wave, in its first appearance, extensively changes the nearby background wave. In the top panel of Fig. 9, the manifestation of a variety of wave groups is clearly visible. To classify types of the wave forms, we conduct a local-IST analysis. We take a cross section of the wave envelop at $z = 46$ as shown in the midpanel of Fig. 9. This is similar to the analysis we carried out earlier in the case of the TOD effect. We select various localized structures from the envelop highlighted in the shaded areas and group them in two separate category according to the genus g . The green

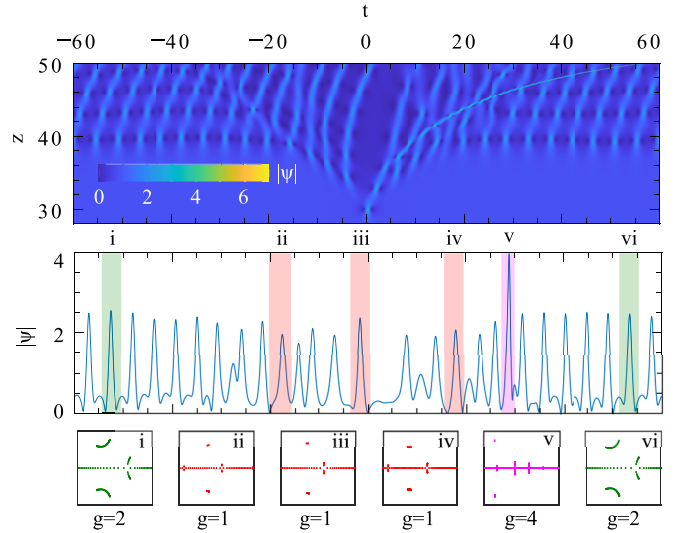


FIG. 9. Top panel: Temporal amplitude evolution of a rogue wave solution under the influence of the RIFS effect. A skewed background wave is visible with a various types of wave entities appearing atop. Midpanel: An extracted wave envelop at $z = 40$ after the emergence of rogue wave. Bottom panel: Local-IST spectra of various localized wave profiles.

shaded areas are breather-type, ($g = 2$) localized structures, and under the red and magenta-shaded areas are the soliton type, where $g = 1$. Note that the transformed soliton which is created from the slow-moving rogue wave is shaded in magenta. The localized structures in (i) and (vi) exhibit three distinct spectral bands, which indicates that they belong to the family of breather-type solutions.

Similar to Fig. 2, the isolated structures in (ii), (iii), and (iv) each appear to have three spectral bands for fixed size windows (shaded areas). The small amplitude-bands crossing the real line arise from the background perturbation.

At this point, we must investigate how the local-IST windowing affects the spectrum and classification of the structure under study. For this, we select the local structure (iii) and change its window by taking three different ranges $(-4, 1)$, $(-5, 2)$, and $(-5, 3)$ in the t axis as shown in Figs. 10(a)–10(c). The choice of the window is restricted within these ranges, because a wider range overlaps with the adjacent structure. Each of them are periodized 100 times [partially presented in Figs. 10(d)–10(f)]. The corresponding local-IST spectra are shown in Figs. 10(g)–10(i), respectively.

When the window size is increased, a small vertical band crossing the real axis grows as shown in the insets in Figs. 10(h) and 10(i), while the conjugates become more focused. This observation is an indication that the conjugate bands arise from the central structure while small bands on the real lines come from the background perturbation. In all three windows, eigenvalues of the conjugate pairs are tightly focused nearly on the same spot, making the structure in Fig. 9 inset (iii) likely to be a $g = 1$ -type solitonlike entity. In a conventional measure, as the structure under investigation is on a constant background, it belongs to $g = 2$ -type solution. However, the complex conjugate bands in (iii) are closely focused nearly at the same spot similar to a regular soliton. We

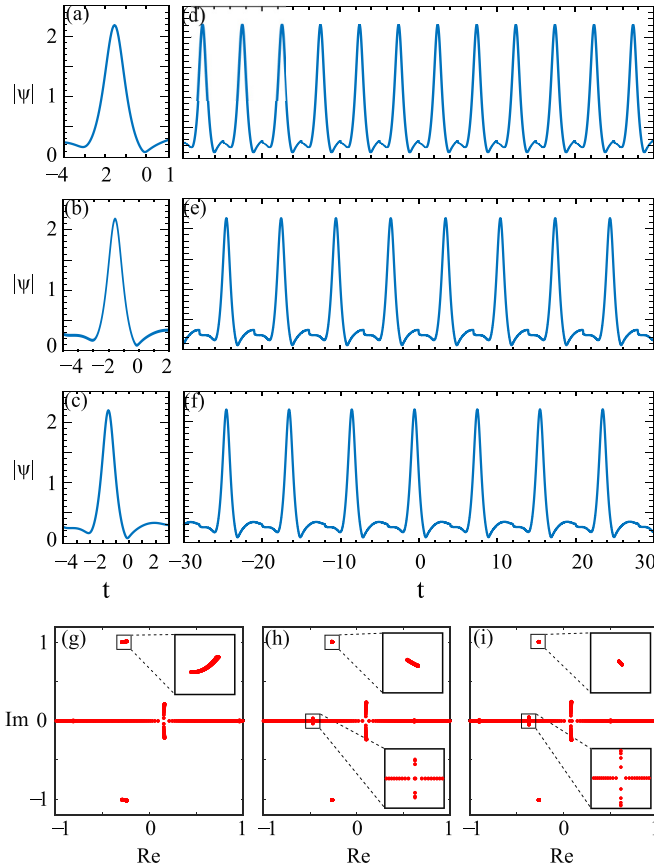


FIG. 10. (a)–(c) are three different window sizes of the structure (iii) in the midpanel from Fig. 9. Corresponding periodization are presented in (d)–(f). Insets (g)–(i) are the respective local-IST spectrums of (d)–(f).

then classify them as a $g = 1$ -type solution. A similar standard of determining the genus is also demonstrated in [38]. See Fig. 7 and the description therein.

The localized structure in Fig. 9(v) is the soliton that is created from the decelerating rogue wave, which has a five local-IST spectral bands making it a $g = 4$ -type solution [32]. Three small irregular bands crossing the real line result from the highly perturbative background. The conjugate eigenvalues are largely shifted away from the imaginary axis due to the asymmetry of the profile.

We conclude that the RIFS effect heavily influences the continuous wave background and triggers a host of other waves such as solitons and breathers. The RIFS effect triggers the formation of a group of low-amplitude solitons around the central region, where the first rogue wave appeared while the rogue wave itself becomes a relatively high-amplitude slow-moving soliton. The breather-type waves form near the edge of the field away from the center.

V. COMBINED EFFECTS

Applying all three effects simultaneously leads to Eq. (1). We solve it numerically to observe their combined influence on the rogue wave solution. The early stage amplitude evolution is shown in Fig. 11 both in temporal and spectral domains,

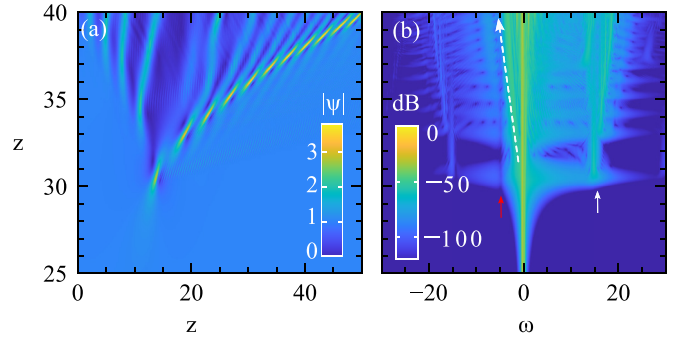


FIG. 11. (a) Temporal and (b) spectral intensity evolutions of the fundamental rogue wave when $\epsilon_3 = -0.03$, $s = 0.2$, and $\tau_R = 0.012$.

which bears a clear signature of the TOD, SS, and RIFS effects. As shown in Fig. 11(a), the SS-induced translation shifts the emergence of rogue wave in the positive t direction. Both the TOD and RIFS effect slow down the rogue wave after its appearance. Their mutual interaction affects the trajectory of rogue wave propagation. This trajectory depends on the magnitude of these two effects.

The TOD onsets the generation of dispersive wave indicated by the white arrow from the first appearance of rogue wave at $z = 30$ as shown in Fig. 11(b). The subsequent emergence of a rogue wave in the extended evolution also radiates dispersive waves. The rogue wave compresses to shorter durations and generates broader spectra further along z . The asymmetry in the spectral profile arises due to the SS and RIFS effects. The SS causes the asymmetry toward the blue, while RIFS produces the red-shifted frequency as shown by the dashed long white arrow. The competing effects cause the total spectral profile to be uneven in the transverse directions.

Note that the spectral discontinuity indicated by the red arrow on the red side of the spectral profile in Fig. 11(b) is also due to the SS effect. The similar spectral gap can be seen to the left of $\omega = 0$ in the analytically obtained spectral profiles in Figs. 5(d) and 5(f) when $s = 0.2$ and $s = 1$.

Finally, we investigate the long-term evolution of the rogue wave under the combined influence. We observe that at the moment of the rogue wave appearance at $z = 30$, it immediately triggers breathers near the edges and a group of low-amplitude solitons around the central part of the propagation field as presented in Fig. 12. At the same time, due to the RIFS effect, the decelerating rogue wave gradually transforms into a soliton as shown in Fig. 12 with a bent trajectory.

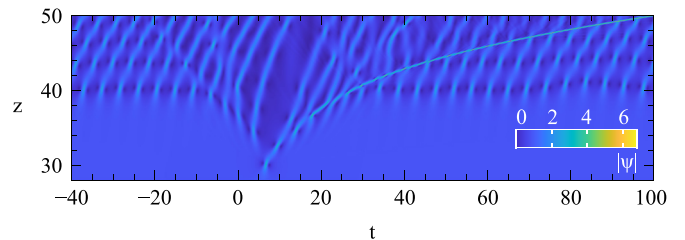


FIG. 12. Decelerating rogue wave under the influence of TOD ($\epsilon_3 = 0.03$), SS ($s = 0.1$), and RIFS ($\tau_R = 0.008$). It transforms into a soliton.

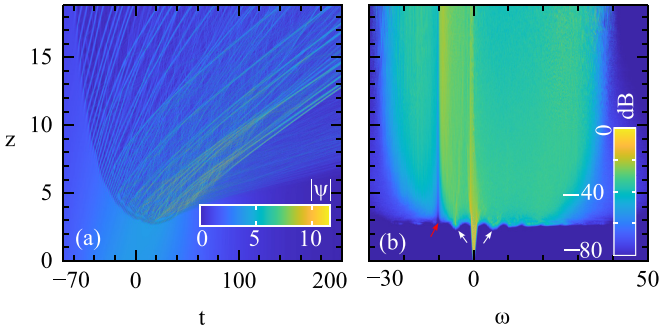


FIG. 13. (a) Temporal and (b) spectral intensity evolutions showing disintegration of $N = 200$ soliton under the influence of TOD ($\epsilon_3 = 0.03$), SS ($s = 0.1$), and RIFS ($\tau_R = 0.001$).

Note that as this soliton is propagating on a modulated wave field, the soliton profile is not uniform. It collides with the surrounding breathers-type waves as it advances and develops ridges on top, as seen in Fig. 12.

To give an example of the implication of the current analysis of how rogue waves can trigger the formation of a large number of solitons, we simulated $N = 200$ solitons with TOD ($\epsilon_3 = -0.03$), SS ($s = 0.1$), and RIFS ($\tau_R = 0.001$) using Eq. (1). It is highlighting the processes of continuous wave supercontinuum generation in optical fiber [53]. The evolution dynamics in the temporal domain can be observed in Fig. 13(a). Clearly, the conventional perturbation induced soliton-fission involving a low number of soliton does not take place in this case. Instead, the presence of noise among the closely packed high number of solitons triggers the onset of MI, which in its initial stage gradually amplifies along the evolution. When the growth of MI is at its peak value, first, it creates a large number of highly compressed rogue-wave-type localized structures.

Under the influence of the combined effects, in the final stage, these localized structures deliver a shower of solitons moving toward the positive t direction. These ejected solitons have a close dynamical resemblance to the solitons that we discussed in Fig. 12 under the combined effects of TOD, SS, and RIFS. The evidence of the onset of MI is clearly seen in the spectral profile Fig. 13(b) with the presence of side lobes indicated by the white arrows. Moreover, a spectral gap is observed next to the left side-lobe that arises from the SS effect shown by the red arrow.

VI. CONCLUSION

We studied the dynamical properties of a fundamental rogue wave under the influence of TOD, SS, and RIFS effects. We showed these effects acting on the rogue wave separately as well as simultaneously. In a real system, hundreds of rogue wave-type structures are formed due to MI. The purpose of this article is, in light of the systematic analysis of one of them, to explain their collective behavior in a system where they may arise.

We revealed the key mechanisms of TOD, SS, and RIFS effects that can significantly impact an optical rogue wave's long-time behavior on a continuous wave background. Using numerical analysis, complemented with a local-IST procedure,

we explain how these three effects play key roles in producing multiple soliton-type structures from the modulated wave background.

Under the TOD effects, the dynamics of the standard breather solution can trigger the formation of solitonlike structures together with modified breathers and new rogue-wave-type formations in its surroundings. To confirm the nature of the developed localized structures, we employed the local-IST procedure to reveal their spectra. We found that the soliton-type structures are triggered from the central area where the rogue wave solution first appeared. New breather and rogue wave-type localized structures are formed near the edges.

We observed similar dynamics under the RIFS effect too. However, the major revelation here is that, after its appearance the rogue wave solution itself gradually slows-down via radiating a continuous red-shifted frequency components. While decelerating, it loses energy and slowly transforms into a high-amplitude soliton.

Using the rogue wave solution volume interpretation, we showed that under the SS effect, the rogue wave becomes stretched by reducing its volume. The SS effects can act like a catalyst, stimulating rogue waves to turning into a soliton. Importantly, we showed that this effect can relocate the emerging point of the rogue wave solution in the transverse dimension. We also observed that the SS effect induces an instantaneous spectral change in the rogue waves' spectrum.

When these three effects were applied simultaneously, after an extended period of propagation, we observed the creation of a collection of solitons that corresponds to an asymmetric spectral profile. Both the spectral and temporal profiles show the signatures of all three effects. By simulating 200 solitons, we demonstrated that the rogue waves shaped by the noise-driven MI finally become an ensemble of solitons.

We believe these observations present a coherent overview of long-term continuous wave propagation inside an optical fiber. As a representative case, the observation revealed how MI leads to the formation of rogue waves at the initial stage of continuous wave supercontinuum generation, which at the final stage transforms into a large collection of soliton-type structures. Also, a comprehensive understanding of the first-order rogue wave solution evolution in the presence of the higher-order effects may shed light on propagation dynamics of the higher-order rogue wave solutions. The application of a local-IST procedure to investigate how the symmetry-breaking effects changes the local-IST spectrums of the local-periodized structure may provide insights of the dynamics that arise in experiments. We observe that higher-order optical effects locally change the genus of the solutions under investigation, which currently remains a field of active research. These open questions may stimulate more debates and discussions, leading toward more concrete answers to these questions.

ACKNOWLEDGMENTS

This work is supported by Ministry of Education, Singapore (No. 2019-T2-2-026). A.C. and M.B. acknowledge financial support from the Nanyang Technological University, NAP-SUG.

- [1] K. Dysthe, H. E. Krogstad, and P. Müller, Oceanic rogue waves, *Annu. Rev. Fluid Mech.* **40**, 287 (2008).
- [2] N. Akhmediev, A. Ankiewicz, and M. Taki, Waves that appear from nowhere and disappear without a trace, *Phys. Lett. A* **373**, 675 (2009).
- [3] M. Onorato, A. R. Osborne, M. Serio, and S. Bertone, Freak Waves in Random Oceanic Sea States, *Phys. Rev. Lett.* **86**, 5831 (2001).
- [4] P. Müller, C. Garrett, and A. Osborne, Rogue waves, *Oceanography* **18**, 66 (2005).
- [5] B. Kibler, J. Fatome, C. Finot, G. Millot, F. Dias, G. Genty, N. Akhmediev, and J. M. Dudley, The Peregrine soliton in nonlinear fibre optics, *Nat. Phys.* **6**, 790 (2010).
- [6] W. Moslem, P. Shukla, and B. Eliasson, Surface plasma rogue waves, *Europhys. Lett.* **96**, 25002 (2011).
- [7] L. Stenflo and M. Marklund, Rogue waves in the atmosphere, *J. Plasma Phys.* **76**, 293 (2010).
- [8] V. B. Efimov, A. N. Ganshin, G. V. Kolmakov, P. V. E. McClintock, and L. P. Mezhov-Deglin, Rogue waves in superfluid helium, *Eur. Phys. J. Spec. Top.* **185**, 181 (2010).
- [9] Y. V. Bludov, V. V. Konotop, and N. Akhmediev, Vector rogue waves in binary mixtures of Bose-Einstein condensates, *Eur. Phys. J.: Spec. Top.* **185**, 169 (2010).
- [10] M. Shats, H. Punzmann, and H. Xia, Capillary Rogue Waves, *Phys. Rev. Lett.* **104**, 104503 (2010).
- [11] W. Moslem, R. Sabry, S. El-Labany, and P. Shukla, Dust-acoustic rogue waves in a nonextensive plasma, *Phys. Rev. E* **84**, 066402 (2011).
- [12] Y.-Y. Tsai, J.-Y. Tsai, and I. Lin, Generation of acoustic rogue waves in dusty plasmas through three-dimensional particle focusing by distorted waveforms, *Nat. Phys.* **12**, 573 (2016).
- [13] G. Veldes, J. Borhanian, M. McKerr, V. Saxena, D. Frantzeskakis, and I. Kourakis, Electromagnetic rogue waves in beam-plasma interactions, *J. Opt.* **15**, 064003 (2013).
- [14] Y. V. Bludov, V. V. Konotop, and N. Akhmediev, Matter rogue waves, *Phys. Rev. A* **80**, 033610 (2009).
- [15] Y. Zhen-Ya, Financial rogue waves, *Commun. Theor. Phys.* **54**, 947 (2010).
- [16] N. Akhmediev, V. Eleonsky, and N. Kulagin, Generation of periodic trains of picosecond pulses in an optical fiber: Exact solutions, *Sov. Phys. JETP* **62**, 894 (1985).
- [17] B. Kibler, A. Chabchoub, and H. Bailung, Peregrine soliton and breathers in wave physics: Achievements and perspectives, *Front. Phys.* **9**, 695 (2021).
- [18] M. Onorato, S. Residori, U. Bortolozzo, A. Montina, and F. T. Arecchi, Rogue waves and their generating mechanisms in different physical contexts, *Phys. Rep.* **528**, 47 (2013).
- [19] I. Teutsch, R. Weisse, J. Moeller, and O. Krueger, A statistical analysis of rogue waves in the southern north sea, *Nat. Hazards Earth Syst. Sci.* **20**, 2665 (2020).
- [20] D. R. Solli, C. Ropers, P. Koonath, and B. Jalali, Optical rogue waves, *Nature (London)* **450**, 1054 (2007).
- [21] A. Chabchoub, N. P. Hoffmann, and N. Akhmediev, Rogue Wave Observation in a Water Wave Tank, *Phys. Rev. Lett.* **106**, 204502 (2011).
- [22] N. Akhmediev, J. M. Dudley, D. R. Solli, and S. K. Turitsyn, Recent progress in investigating optical rogue waves, *J. Opt.* **15**, 060201 (2013).
- [23] Y. Song, Z. Wang, C. Wang, K. Panajotov, and H. Zhang, Recent progress on optical rogue waves in fiber lasers: Status, challenges, and perspectives, *Adv. Photon.* **2**, 024001 (2020).
- [24] G. P. Agrawal, Nonlinear fiber optics: Its history and recent progress [invited], *J. Opt. Soc. Am. B* **28**, A1 (2011).
- [25] G. P. Agrawal, *Nonlinear Fiber Optics*, 5th ed. (Elsevier, Amsterdam, 2012).
- [26] A. Ankiewicz, N. Devine, and N. Akhmediev, Are rogue waves robust against perturbations? *Phys. Lett. A* **373**, 3997 (2009).
- [27] U. Bandelow and N. Akhmediev, Persistence of rogue waves in extended nonlinear Schrödinger equations: Integrable Sasa-Satsuma case, *Phys. Lett. A* **376**, 1558 (2012).
- [28] A. Ankiewicz, A. Chowdhury, N. Devine, and N. Akhmediev, Rogue waves of the nonlinear Schrödinger equation with even symmetric perturbations, *J. Opt.* **15**, 064007 (2013).
- [29] A. Ankiewicz, J. M. Soto-Crespo, M. A. Chowdhury, and N. Akhmediev, Rogue waves in optical fibers in presence of third-order dispersion, self-steepening, and self-frequency shift, *J. Opt. Soc. Am. B* **30**, 87 (2013).
- [30] P. S. J. Russell, P. Hölzer, W. Chang, A. Abdolvand, and J. C. Travers, Hollow-core photonic crystal fibres for gas-based nonlinear optics, *Nat. Photon.* **8**, 278 (2014).
- [31] J. C. Travers, W. Chang, J. Nold, N. Y. Joly, and P. S. J. Russell, Ultrafast nonlinear optics in gas-filled hollow-core photonic crystal fibers, *J. Opt. Soc. Am. B* **28**, A11 (2011).
- [32] S. Randoux, P. Suret, and G. El, Inverse scattering transform analysis of rogue waves using local periodization procedure, *Sci. Rep.* **6**, 29238 (2016).
- [33] A. Atieh, P. Myslinski, J. Chrostowski, and P. Galko, Measuring the raman time constant (T_R) for soliton pulses in standard single-mode fiber, *J. Lightwave Technol.* **17**, 216 (1999).
- [34] V. E. Zakharov and A. B. Shabat, Exact theory of two-dimensional self-focusing and one-dimensional self-modulation of waves in nonlinear media, *J. Exp. Theor. Phys.* **34**, 62 (1972).
- [35] N. Akhmediev, A. Ankiewicz, and J. M. Soto-Crespo, Rogue waves and rational solutions of the nonlinear Schrödinger equation, *Phys. Rev. E* **80**, 026601 (2009).
- [36] A. Chowdury and W. Chang, Rogue wave fission, *Phys. Rev. Res.* **3**, L032060 (2021).
- [37] S. Randoux, P. Suret, A. Chabchoub, B. Kibler, and G. El, Nonlinear spectral analysis of peregrine solitons observed in optics and in hydrodynamic experiments, *Phys. Rev. E* **98**, 022219 (2018).
- [38] F. Bonnefoy, A. Tikan, F. Copie, P. Suret, G. Ducrozet, G. Prabhudesai, G. Michel, A. Cazaubiel, E. Falcon, G. El *et al.*, From modulational instability to focusing dam breaks in water waves, *Phys. Rev. Fluids* **5**, 034802 (2020).
- [39] F. Baronio, S. Chen, and S. Trillo, Resonant radiation from peregrine solitons, *Opt. Lett.* **45**, 427 (2020).
- [40] B. Kibler, K. Hammani, C. Michel, C. Finot, and A. Picozzi, Rogue waves, rational solitons and wave turbulence theory, *Phys. Lett. A* **375**, 3149 (2011).
- [41] M. Taki, A. Mussot, A. Kudlinski, E. Louvergneaux, M. Kolobov, and M. Douay, Third-order dispersion for generating optical rogue solitons, *Phys. Lett. A* **374**, 691 (2010).
- [42] N. Akhmediev and M. Karlsson, Cherenkov radiation emitted by solitons in optical fibers, *Phys. Rev. A* **51**, 2602 (1995).

- [43] S. Xu, J. He, and L. Wang, The Darboux transformation of the derivative nonlinear Schrödinger equation, *J. Phys. A: Math. Theor.* **44**, 305203 (2011).
- [44] C. Liu and N. Akhmediev, Super-regular breathers in nonlinear systems with self-steepening effect, *Phys. Rev. E* **100**, 062201 (2019).
- [45] H. N. Chan, K. W. Chow, D. J. Kedziora, R. H. J. Grimshaw, and E. Ding, Rogue wave modes for a derivative nonlinear Schrödinger model, *Phys. Rev. E* **89**, 032914 (2014).
- [46] S.-H. Han and Q.-H. Park, Effect of self-steepening on optical solitons in a continuous wave background, *Phys. Rev. E* **83**, 066601 (2011).
- [47] S. Chen, F. Baronio, J. M. Soto-Crespo, Y. Liu, and P. Grelu, Chirped peregrine solitons in a class of cubic-quintic nonlinear Schrödinger equations, *Phys. Rev. E* **93**, 062202 (2016).
- [48] S. Chen, Y. Zhou, L. Bu, F. Baronio, J. M. Soto-Crespo, and D. Mihalache, Super chirped rogue waves in optical fibers, *Opt. Express* **27**, 11370 (2019).
- [49] A. Ankiewicz and N. Akhmediev, Multi-rogue waves and triangular numbers, *Rom. Rep. Phys.* **69**, 104 (2017).
- [50] A. Ankiewicz and A. Chowdury, Analysis of characteristics of rogue waves for higher-order equations, *Nonlin. Dyn.* **109**, 1069 (2022).
- [51] C. R. Menyuk, Soliton robustness in optical fibers, *J. Opt. Soc. Am. B* **10**, 1585 (1993).
- [52] J. M. Soto-Crespo, N. Devine, and N. Akhmediev, Integrable Turbulence and Rogue Waves: Breathers or Solitons? *Phys. Rev. Lett.* **116**, 103901 (2016).
- [53] *Supercontinuum Generation in Optical Fibers*, edited by J. M. Dudley and J. R. Taylor (Cambridge University Press, Cambridge, NY, 2010).